

NJC

Accepted Manuscript



This is an *Accepted Manuscript*, which has been through the Royal Society of Chemistry peer review process and has been accepted for publication.

Accepted Manuscripts are published online shortly after acceptance, before technical editing, formatting and proof reading. Using this free service, authors can make their results available to the community, in citable form, before we publish the edited article. We will replace this *Accepted Manuscript* with the edited and formatted *Advance Article* as soon as it is available.

You can find more information about *Accepted Manuscripts* in the [Information for Authors](#).

Please note that technical editing may introduce minor changes to the text and/or graphics, which may alter content. The journal's standard [Terms & Conditions](#) and the [Ethical guidelines](#) still apply. In no event shall the Royal Society of Chemistry be held responsible for any errors or omissions in this *Accepted Manuscript* or any consequences arising from the use of any information it contains.



Journal Name

ARTICLE

Influence of the porous texture of SBA-15 mesoporous silica on the anatase formation in TiO₂ – SiO₂ nanocomposites

Manon Besançon,^a Laure Michelin,^a Ludovic Josien,^a Loïc Vidal,^a Karine Assaker,^b Magali Bonne,^{*a} Bénédicte Lebeau,^{*a} Jean-Luc Blin^b

Received 00th January 20xx,
Accepted 00th January 20xx

DOI: 10.1039/x0xx00000x

www.rsc.org/

Two series of TiO₂ – SiO₂ composites have been prepared by post-synthesis impregnation of a TiO₂ precursor onto SBA-15 silica matrices and a subsequent thermal treatment at 400 °C under air. The influence of the textural properties of the SBA-15 and the TiO₂ content was evaluated on the dispersion of TiO₂ and its crystallization in anatase. The morphology of the samples before and after impregnation was observed by electronic microscopy while the textural and structural properties were evaluated by different techniques such as XRD, nitrogen sorption manometry, Raman spectroscopy. The quantity of crystallized anatase in the composites was determined by a XRD quantification using an internal standard. The bandgap energy (E_g) of the composites were evaluated by diffuse reflectance spectroscopy and results show that E_g decreases as a function of the titania content. The photoactivity of the prepared materials was evaluated by following the degradation of methyl orange (MO) in water under UV irradiation. For the same amount of catalyst, the MO degradation rate in presence of the composites containing 28 and 44 wt% of crystallized anatase was found similar to the one in the presence of a commercial fully crystallized anatase.

Introduction

Nowadays, the increasing interest in heterogeneous photocatalysis leads to the study and development of new photocatalysts. Indeed, water and air treatments, bacterial studies ... using photocatalysis are more and more developed¹⁻³. Among all the photocatalysts studied, TiO₂ semi-conductor is one of the most used⁴. Titania exists as different polymorphs, the most known are brookite, anatase and rutile phases, presenting different physical properties⁵. Among these common crystalline forms of titania, due to its strong oxidizing properties and long term photostability, anatase is generally recognized to be the most active phase for photocatalysis^{6,7}. Photocatalytic efficiency is favoured by an increase of the crystalline degree, the particle size, the specific surface area

and the porosity^{8,9}. Lots of studies are developed in order to synthesize nanotubes of TiO₂ or mesoporous TiO₂ for increasing the titania specific surface area or to make possible the introduction of an active phase in the pores¹⁰⁻¹³. However, compared to silica materials it is difficult to obtain TiO₂ with stable mesostructure and the main challenge is to preserve the pore ordering upon surfactant removal. The other key parameter for the formation of titania with a mesopore ordering concerns the control of the titanium precursor hydrolysis and condensation as well as the aging process. As a matter of fact precursors such as titanium alkoxides or titanium chloride exhibit a high reactivity towards hydrolysis and condensation. As a consequence, dense TiO₂ with a poor mesopore arrangement is often recovered.

To enhance the photocatalytic activity of titania, different studies have been developed where titania is doped with metal ions or where mixed oxides are synthesized¹⁴⁻¹⁶. In particular, TiO₂ – SiO₂ mixed oxides exhibit a high thermal stability and mechanical strength; both properties come from silica, as well as good optical and catalytic properties, provided by the TiO₂ phase. Moreover, due to its properties such as high specific surface area, mesostructured silica is an excellent candidate as host support for titania. In addition to its textural properties, mesostructured silica is thermally stable and so can be used in many application fields. By this way, the advantages of the silica support (e.g. opened porosity, thermal stability) and the properties of Ti clusters are combined in order to improve the catalytic activity of TiO₂. Another advantage of the TiO₂ - SiO₂ mixed oxides concerns the delay in the anatase to rutile phase transition^{17,18}. The use of a silica host support thus

^a. Université de Haute Alsace, CNRS, Equipe Matériaux à Porosité Contrôlée, Institut de Science des Matériaux de Mulhouse, UMR 7361, ENSCMu, 3bis rue Alfred Werner, F-68093 Mulhouse cedex, France. E-mail: magali.bonne@uha.fr, benedicte.lebeau@uha.fr

^b. SRS MC UMR 7565, Université de Lorraine, CNRS, F-54506 Vandoeuvre-lès-Nancy cedex, BP 70239, France. E-mail: jean-luc.blin@univ.lorraine.fr

† Electronic Supplementary Information (ESI) available: Structural and textural properties of the different mesoporous hosts (Table S1). XRD patterns of the anatase phase and the internal standard chosen (Fig.S1). Calibration line obtained with the standard mixtures (Fig. S2). SEM images of the SBA-15 type ordered mesoporous silicas synthesized at 36 °C (A), 60 °C (B), 90 °C (C) and 130 °C (D) (Fig. S3). TEM images with bright and dark field mode of 50Ti@60 (left) and 50Ti@90 (right) (Fig. S4). Low-angles XRD patterns of a physical mixture (50 wt% of TiO₂ and SBA-15) and the composite 50Ti@130 (Fig.S5). TEM images with bright and dark field mode of 25Ti@130 (left) and 80Ti@130 (right) (Fig.S6). . (αhν)² versus photon energy (hν) for the different composites of series b (Fig.S7) See DOI: 10.1039/x0xx00000x

appears as an alternative way to nanostructure titania for catalytic applications.

TiO₂ – SiO₂ mixed oxides have been prepared according to different methods: by sol-gel process with co-condensation of titania and silica sources¹⁹⁻²⁴ or by different post grafting processes²⁵⁻³⁰. For example, Lihitkar *et al.* have obtained TiO₂ nanoparticles embedded within the MCM-41 mesopores by the impregnation method²⁷. The authors have reported that titania particles of an average size of 3 nm are obtained and that the titania particles are coordinated with silica MCM-41 by Si-O-Ti covalent bond.

For direct incorporation of Ti atoms in the silica walls during the synthesis, it is important to control the synthesis conditions and thus avoid the formation of large external Ti particles. For example, Zhao *et al.* have shown that at low content, titanium is incorporated into the framework of SBA-15. With the increase of titanium content, the TiO₂ anatase particles are formed, located on the external surface of SBA-15. The recovered Ti-SBA-15 composites are active for a photocatalytic reaction in water treatment³¹.

By post-grafting TiO₂ on a SiO₂ host support, special attention should be paid to the loading amount of TiO₂ to avoid the pore blocking. It has been demonstrated that incorporation of TiO₂ at low loadings leads to good dispersion of Ti atoms in pore structure, and that the catalytic activity depends on the size of formed TiO₂ clusters. Comparing the direct to the post synthesis methods, the first one results in a relatively homogeneous incorporation of the titanium, whereas the post synthesis procedure leads to an increase of the titanium concentration on the surface²⁵.

Thanks to their characteristics, these oxides were used as good photocatalysts as well as support material for other heterogeneous catalysts³²⁻³⁷. Indeed, many researchers have reported on the preparation and properties of selective catalytic oxidation of various Ti-containing mesoporous materials, such as Ti-MCM-41^{38,39}, Ti-MCM-48⁴⁰, Ti-SBA-15⁴¹, Ti-HMS⁴², ... More recently, the impact of TiO₂ dispersed in a silica SBA-15 support and its influence on the activity of the CoMo catalysts in the hydrodesulfurization reaction were studied. An intermediate TiO₂ content of 20 wt% was determined to optimize active phase particles dispersion on the support and preserve intrinsic activity of the active sites³⁷.

In particular, the use of SBA-15 mesoporous silica as a host support for preparation of SiO₂ – TiO₂ composites has been largely studied and described in the literature⁴³⁻⁴⁷ and their photocatalytic activity have been studied⁴⁸⁻⁵¹. Indeed, in recent developments of photocatalytic materials regarding semiconductor TiO₂, metallic nanostructures in mesoporous silica frameworks were suggested for environmental remediation and solar energy utilization. The advantages of mesoporous-silica-based hosts are numerous, but the main important could be:

- 1) a large nanospace provided;
- 2) possibility of anchoring functional groups and moieties in order to create a unique photocatalytic reactor;
- 3) possible control of the diffusion, the nature and size of the photo-responsive components⁵².

In this work, different TiO₂ – SiO₂ composites were prepared by dispersing TiO₂ in SBA-15 type mesoporous silica. The choice of SBA-15 mesoporous silica as host support has been made because of the mesopores diameter which is in the range of 5 – 10 nm and also because it exhibits better thermal and hydrothermal stability compared to MCM-41 mesoporous silica. Composites of different TiO₂/SiO₂ mass ratios were prepared using a large pore SBA-15 host support, but also composites with the same TiO₂/SiO₂ mass ratios using SBA-15 host supports with different pore diameters. All the composites were prepared by post impregnation of SBA-15 support using a TiO₂ precursor diluted in alcohol and a subsequent thermal treatment at 400 °C under air. The materials were then finely characterized in order to have a precise description of the composites¹³. The objective of the study is to obtain nanoparticles of titania well dispersed inside the porosity of the silica support. The influence of the mean pore size of the supports is studied and the quantity of crystallized anatase in each sample was determined by XRD quantification using an internal standard. This original method allows us to measure the quantity of anatase formed during the calcination process which can be different from the initial quantity of Ti precursor impregnated. Moreover this quantification will allow us to correlate the influence of the porous texture of the silica host support on the formation of anatase nanocrystals. Finally, the possible catalytic activity of the composites was evaluated by studying the photodegradation of methyl orange (MO) in water under UV irradiation.

Experimental part

Syntheses

Synthesis of the host supports (SBA-15).

Triblock copolymer P123 (EO)₂₀(PO)₇₀(EO)₂₀ used as structure directing agent was purchased from Aldrich. TetraEthylOrthoSilicate (TEOS) and Titanium Isopropoxide (Ti(OⁱPr)₄) from Aldrich were used as inorganic precursors.

The SBA-15 supports were synthesized according to the protocol described by Zhao *et al.*⁵³. In a polypropylene bottle, P123 was dissolved in an acidic medium of concentrated hydrochloric acid and water. The bottle was placed in a water bath at 40 °C in order to allow a complete dissolution of P123. Then TEOS was added by maintaining the temperature conditions. The molar composition of the gel was 1 TEOS: 0.017 P123: 5.68 HCl: 197 H₂O. The solution was stirred during 2 hours under these conditions and then transferred to the oven for 24 hours at a temperature comprised between 36 and 130 °C (called synthesis temperature). It is noteworthy that the synthesis at 130°C was realized in an autoclave. After filtration and washing on a Buchner funnel the solid was dried at 70 °C for 24 hours. In order to release the porosity, the solid was calcined in a muffle furnace at 300 °C for 4 hours (temperature increasing time: 6 hours).

Four different supports were synthesized at ageing temperatures of 36, 60, 90 and 130 °C for the different composites.

TiO₂ – SiO₂ composite synthesis

Two series of TiO₂-SiO₂ composites have been prepared. The series a corresponds to composites made with 50 wt% of TiO₂ from SiO₂ SBA-15 hosts synthesized at 36, 60, 90 and 130 °C. The series b consists of composites with different TiO₂ loadings of 10, 25, 50, 70 and 80 wt% prepared from the same SiO₂ SBA-15 host synthesized at 130 °C. The different composites were prepared by impregnation in an excess of solvent. A known volume (depending on the desired titania loading) of Ti(OⁱPr)₄ was diluted in 20 mL of dry ethanol and slowly added to the silica support in order to prepare 1 g of TiO₂ – SiO₂ composite. The solvent is evaporated under stirring at room temperature and the solid is dried at 70 °C for one night. For TiO₂ content superior to 50 wt% the impregnation procedure is repeated a second time to obtain the desired TiO₂ content. The TiO₂ loading vary from 10 to 80 wt%. The composite is then calcined at 400 °C under air during 4 hours (temperature increasing time: 6 hours) in order to obtain the anatase phase. The nomenclature used for the composites is defined as follows:



with: X = TiO₂ content (in wt%), Y = synthesis temperature (°C) and n = a or b series.

It is noteworthy that two composites with 50 wt% of TiO₂ and a host support synthesized at 130 °C have been prepared: 50Tia@130 and 50Tib@130.

Materials characterization

The morphology of the supports and the composites as well as the Ti and Si distributions were observed by Scanning Electron Microscopy (Philips FEG XL30) coupled with Energy Dispersive X-ray Spectroscopy (EDS). The samples were first metalized by a thin carbon layer.

The pore structure of the different samples, as well as TiO₂ nanoparticles, were observed by Transmission Electronic Microscopy (TEM). Micrographs were obtained using a Philips CM200 working at 200 kV.

Powder low- and wide-angle XRD patterns were recorded on a PANalytical X'Pert Pro (45kV, 40mA) using a Cu K α (λ = 1.5418 Å) as the X-ray source. The signal was recorded for 2θ = 0.5 – 10 ° with a step of 0.02 °.s⁻¹ at low angles, and for 2θ = 10 – 70 ° with a step of 0.02 °.s⁻¹ at wide angles.

Specific surface area, pore size distribution and pore volume were obtained from nitrogen adsorption/desorption experiments. A known mass of sample were first degassed at 150 °C under 1.33 Pa overnight. Isotherms were collected at -196 °C on a Micromeritics Tristar equipment.

The specific surface area of the samples was determined using the linear part of the BET plot and the pore size was estimated using the desorption branch of the isotherms using the Barrett – Joyner – Halenda (BJH) model although it is well known that this method gives an underestimated pore size and that some new methods have been developed⁵⁴. We use it here for the sake of simplicity and the use of this mathematical algorithm does not affect significantly our results as it is a systematic comparison. The microporous volume is extrapolated from the linear part of the t-plots

The Raman spectroscopic measurements were performed at room temperature with a FRA106/S FT-Raman module attached to a Bruker Equinox 55 FT-IR spectrometer equipped with a Nd:YAG laser operating at 1064 nm and a Ge detector. The spectra were collected using an output laser power of 400 mW and a spectral resolution of 4 cm⁻¹.

Diffuse reflectance UV-Vis spectra were obtained in air and under ambient conditions using a PerkinElmer Lambda 35 spectrometer equipped with an integrated sphere (Labsphere RSA-PE-20) for solid samples.

The quantity of crystallized anatase (wt%) in each sample was determined by XRD quantification using an internal standard. The reflexion (2 0 0) at 48.04 °2 θ has been chosen for the study because it corresponds to the first most intense and isolated peak, which is not in the region of the amorphous SiO₂ signal. The internal standard chosen is α -Al₂O₃ (corundum, Fluka) due to the presence of an intense peak (reflexion (1 1 3) at 43.35 °2 θ) close to the studied one on anatase XRD pattern with no possible overlapping (Fig. S1).

Physical mixtures of anatase 10 nm (Alfa Aesar) and calcined SBA-15 (series a aged at 130 °C) have been prepared in order to make standard compositions. For each XRD pattern, recordings were made at constant mass and volume, in the following mass proportions: 1/3 internal standard and 2/3 sample. A calibration line was made with the different standard mixtures at 10, 20, 40, 60, 80 and 100 wt% TiO₂ (Fig. S2).

Photocatalytic activity

Methyl orange (MO) was chosen as the organic compound to evaluate the photocatalytic properties of the different nanocomposites synthesized. Analyses have been performed according to the previously published procedure³². 50 mg of composite (or commercial anatase 10 nm purchased from Alfa Aesar, or P25 from Evonik) have been added to 100 mL of an aqueous MO solution (16 mg L⁻¹). The reaction was carried out under continuous stirring in a quartz flask. The resulting suspension was left 1h in the dark to equilibrate the system prior irradiation. The UV-VIS spectra of the initial MO solution and the suspension prior irradiation are similar indicating that no MO was adsorbed on the catalyst.

Samples were irradiated with UV light from a high-mercury lamp. The irradiation was assured by artificial light using a mercury lamp (low pressure mercury arc, USHIO, light power 7 W) emitting in the near-UV. The mean value of the radiation power impinging on the reacting suspension was estimated to be $I_{\text{incident}} = 10^{-5}$ Einstein L⁻¹ s⁻¹. The degradation process of MO was monitored using a Cary 3E UV-Vis-spectrophotometer. The photocatalytic degradation of MO in solution was followed by measuring the absorbance value at $\lambda = 464$ nm, which allowed access to the MO concentration. Analytical uncertainty on MO concentration was mainly due to the filtration step (performed on the suspension MO aqueous solution/catalyst with YY filter) and has been evaluated to be 1.5 mg L⁻¹.



Journal Name

ARTICLE

Table 1. Structural and textural properties of the different composites

Sample	$S_{\text{BET}}^a / \text{m}^2 \cdot \text{g}^{-1}$	$V_{\text{meso}}^a / \text{cm}^3 \cdot \text{g}^{-1}$	$V_{\text{micro}}^a / \text{cm}^3 \cdot \text{g}^{-1}$	D_p^a / nm	a_0^b / nm
50Tia@36	311	0.16	0.06	3.7	9.2
50Tia@60	424	0.25	0.08	3.4	9.7
50Tia@90	362	0.25	0.06	4	10.3
50Tia@130	537	0.44	0.04	3.8	11.1
10Tib@130	580	1.10	0.03	7.6	11.5
25Tib@130	495	0.83	0.02	6.3	11.4
50Tib@130	397	0.52	0.01	4.9	11.2
70Tib@130	261	0.36	0.00	4.6	11.1
80Tib@130	163	0.21	0.00	4.3	-

^a S_{BET} is the specific surface area obtained using the BET model, V_{micro} is the microporous volume extrapolated from the t-plots, $V_{\text{meso}} = V_{\text{tot}} - V_{\text{micro}}$ is the mesopore volume where V_{tot} is the total pore volume obtained at $P/P_0 = 0.9$, D_p is the mean pore diameter obtained using the BJH model on the desorption branch.

^b a_0 is the lattice parameter calculated for a 2D hexagonal system, $a_0 = (2d_{100})/\sqrt{3}$, where d_{100} is the lattice spacing obtained using low angle XR

Results and discussion

SBA-15 host supports

The N_2 sorption isotherms of the different host supports are reported in Fig. 1 and the corresponding textural properties are presented Table 1. Whatever the ageing temperature during the synthesis, the SBA-15 type OMS (ordered mesoporous silica) isotherms are all of type IV according to IUPAC classification⁵⁵. The N_2 sorption isotherms of OMS synthesized at a temperature inferior or equal to 90 °C are also type I indicating the presence of microporosity. Indeed these materials are characterized by main cylindrical mesopores arranged in a 2D-hexagonal packing and micropores due to the interpenetration of PEO chain in the silica network. The SBA-15 host synthesized at 90 °C has also secondary small mesopores and/or supermicropores that interconnect primary mesopores. As a result, these materials present high specific surface area and large pore volumes. The SBA-15 host synthesized at 130 °C is characterized by large primary mesopores interconnected by secondary mesopores. The absence of micropores in this material explains in part the lower specific surface area. The XRD patterns obtained in the low 2θ region clearly show three diffraction peaks, characteristic of the (1 0 0), (1 1 0) and (2 0 0) diffraction planes of the 2D hexagonal pore structure (Fig. 1). This suggests that samples have a well-ordered mesostructure. The corresponding lattice spacings estimated on the (1 0 0) diffraction peak are presented Table 1. As expected, according to Galarneau *et al.*⁵⁶, the pore diameter increases and so the silica walls thickness decreases (not presented here) when the ageing temperature increases. The SEM images of the different SBA-15 host supports are presented Fig. S3. In all cases, the

SBA-15 presents a fiber-like morphology made by micron size rods of about 1 μm (length) and 200 nm (width).

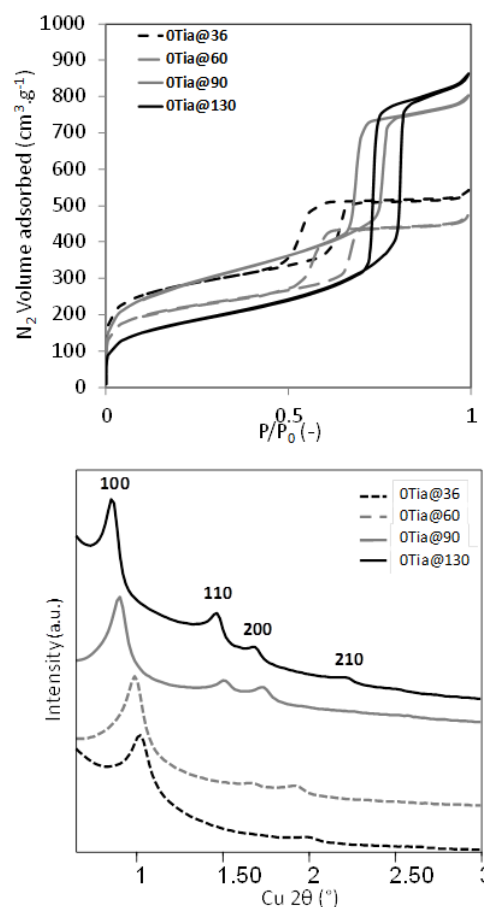


Fig. 1. N_2 adsorption – desorption isotherms (above) and low-angles X-ray diffraction patterns (below) of SBA-15 type mesoporous silicas synthesized after ageing at different temperatures.

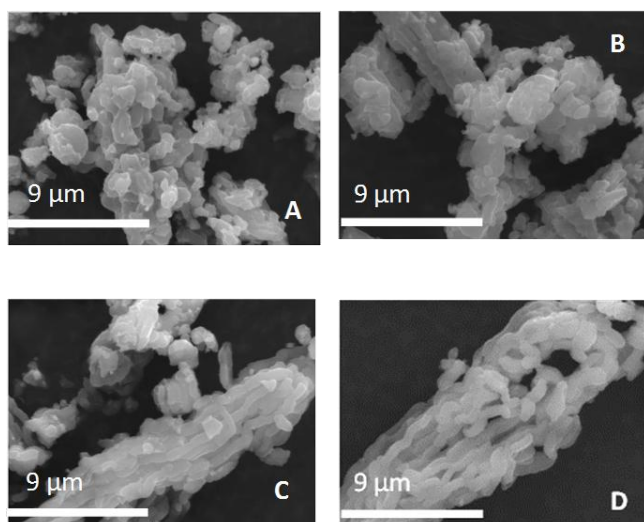
TiO₂ – SiO₂ composites

Fig. 2. SEM images of the 50 wt% TiO₂ – SiO₂ composites (series a) obtained from SBA-15 aged at different temperatures: 50Tia@36 (A), 50Tia@60 (B), 50Tia@90 (C) and 50Tia@130 (D).

By observing the SEM images of the composites of the series a (50 wt% of TiO₂), it appears that in the case of hosts aged at temperature ≥ 90 °C the rod-shape morphology of SBA-15 particles is still observed (Fig. 2C, D). In the case of hosts aged at lower temperatures (36 and 60 °C) the rod-shape morphology is still present but particles with undefined morphology are also observed (Fig. 2A, B). The proportion of these latter increases with decreasing of the synthesis temperature. These changes in morphology can be explained by the formation of TiO₂ outside SBA-15 hosts or by textural modification upon TiO₂ crystallization.

For the composites of series b, the fibre morphology of aggregates and the rod-shape morphology of primary SBA-15 particles is observed for TiO₂ contents ≤ 50 wt% (Fig. 3A, B, C). Some morphology changes were observed when increasing the TiO₂ content (> 50 wt%). For 70Tib@130 rod-like particles are still observed and in major proportion, but other particles with undefined particles are also observed (Fig. 3D). For 80Tib@130, the rod-like morphology is rarely observed and major particles have undefined morphology (Fig. 3E). As observed for the composites of the series a obtained from hosts aged at low temperatures, the crystallization of TiO₂ under thermal treatment at 400 °C has provoked not only structural and textural modifications but also the modification of the silica host morphology. From the TEM observations, the morphology changes can be explained by the formation of aggregates of TiO₂ nanoparticles on the surface of the SiO₂ host and the breakage of the fiber-like aggregates and most of the primary particles of the SBA-15 hosts upon TiO₂

crystallization. In the present case these two phenomena are more extended due to the high TiO₂ content. However the mesostructure of the host SBA-15 particles is globally preserved as observed by TEM (Fig. S4).

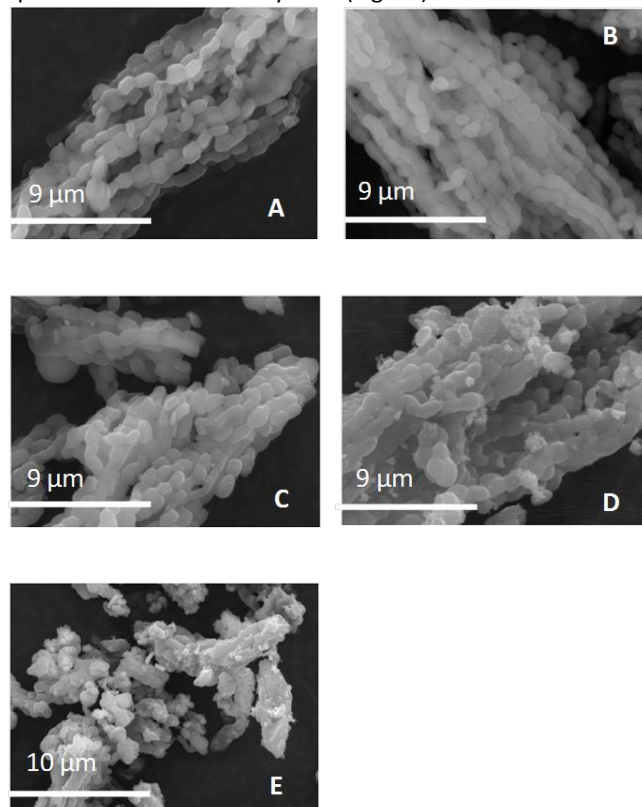


Fig. 3. SEM images of the TiO₂ – SiO₂ composites obtained from SBA-15 aged at 130 °C (series b) with 10 wt% (A), 25 wt% (B), 50 wt% (C), 70 wt% (D) and 80 wt% (E) of TiO₂.

TEM has also revealed the presence of aggregates of TiO₂ nanoparticles on the surface of SBA-15 particles. The particles with undefined morphology may also correspond to the outside formation of TiO₂.

The elemental mapping images displayed in Fig. 4 show the repartition of Ti and Si in some composites. In the case of 10Tib@130, the Ti signal is low due to the small quantity of TiO₂ in the composites. For sample 80Tib@130, all the particles with rod-shape or undefined morphology contains both Si and Ti elements. Whatever the TiO₂ content, it seems that the impregnation method used allows a homogeneous repartition of TiO₂ on the SiO₂ supports. However the low resolution of the elemental mapping does not allow to distinguish individually the particles and to check if the ratio Ti/Si is constant or variable from one particle to another one.

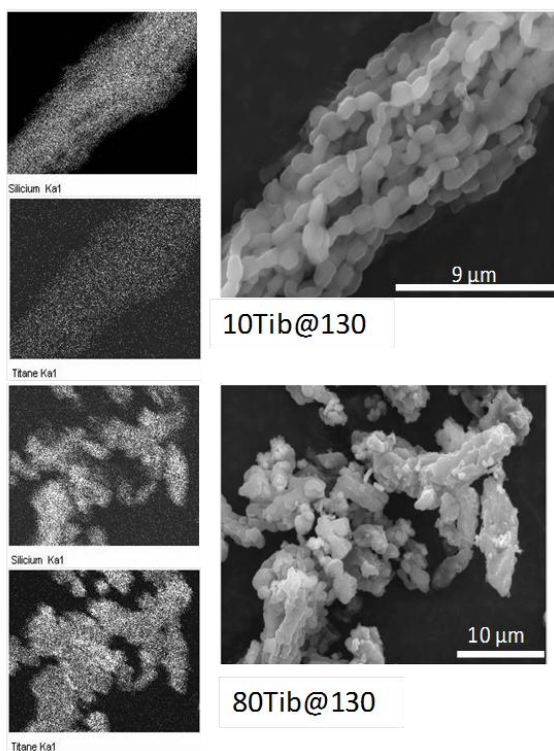


Fig. 4. SEM and corresponding elemental mapping images of 10Tib@130 and 80Tib@130.

The N_2 adsorption - desorption isotherms of the two series of composites are displayed in Fig. 5. The textural characteristics of all composites are reported Table 1. By focusing on the composites of the series a, all isotherms are type IV, but compared to the SBA-15 hosts, the condensation capillary steps are broader due to a larger pore size distribution and the hysteresis are type H2⁵⁵ indicating a partial pore blocking.

The shape of the isotherms is in agreement with the partial filling of main mesopores. The fast desorption at P/P_0 of 0.45 corresponds to the catastrophic emptying of mesopores characteristics of bottle-necked pores. The average pore size measured from the desorption branch is then non indicative. However it is interesting to note that the condensation capillary step on the adsorption branch occurs at lower P/P_0 indicating lower pore sizes than those of the corresponding SBA-15 hosts. These results show that some TiO_2 are inside primary mesopores forming bottlenecks. For composites of the series a (50 wt% TiO_2), it clearly appears that the specific surface area and the pore volumes are lower than those of the host supports. The decrease is more pronounced for composites obtained from a SBA-15 host synthesized at low ageing temperatures ($\leq 90^\circ C$). This is due to the presence of microporosity which is low, indicating a partial micropore filling in the composites. For 50Tia@130, both decrease of the specific surface area and micropore volume is low but the decrease of the mesopore volume is high compared to the SBA-15 host. This means that the pore size of the silica supports, aged at $130^\circ C$ is large enough (about 8 nm) to allow the impregnation inside the mesoposity.

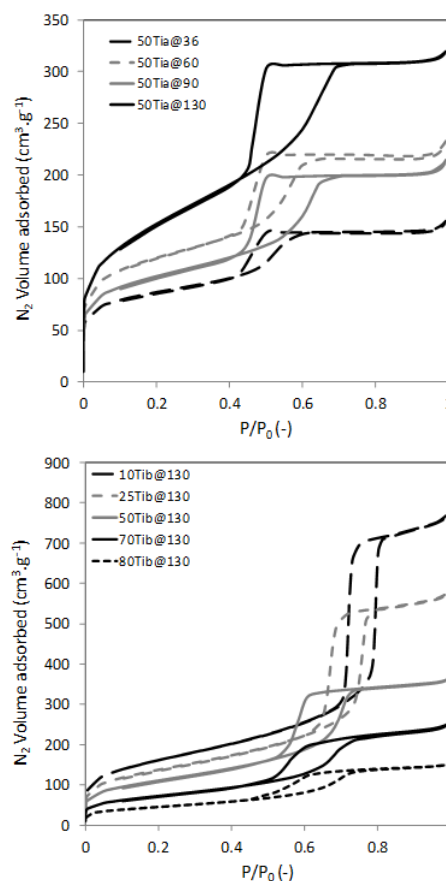


Fig. 5. N_2 adsorption - desorption isotherms of the composites.

Concerning the isotherms of the series b, they are all type IV with H1 type hysteresis⁵⁵ but with different shapes from parent SBA-15 hosts at high TiO_2 contents. By comparing the shapes of the isotherms of the composites 10Tib@130 and 25Tib@130 to the host SBA-15 aged at $130^\circ C$, the same hysteresis of H1 type is observed with a high and thin capillary condensation step.

In these cases it seems that TiO_2 is homogeneously located on the pore surface or outside of the pores, this is in agreement with results reported in the literature indicating that a loading of 20 wt% of TiO_2 is the optimal value for a homogenous dispersion³⁷. The first case is the most probable since the morphology of particles observed by SEM is very similar to the one of the SBA-15 hosts. When increasing TiO_2 content (≥ 50 wt%), the shape of the isotherms change with decreasing and broadening of the capillary condensation step corresponding to larger pore size distributions and decreasing of the mesopore volumes. For the series b of composites prepared from the SBA-15 type OMS aged at $130^\circ C$, the specific surface area, the pore volume and pore diameter decrease when increasing the TiO_2 content. Surprisingly, the specific surface area of the composite 10Tib@130 is higher than the one of the corresponding host. This composite displays also microporosity (micropore volume of $0.03 \text{ cm}^3 \text{ g}^{-1}$ with a micropore specific surface area of about $70 \text{ m}^2 \text{ g}^{-1}$ determined by the t-plot method) which is not the case of

its host. This microporosity can explain the increase of the specific surface area. The presence of microporosity is also observed for composites with 25 and 50 wt%, and is probably attributed to the formation of nanodomains of TiO_2 inside mesopores and/or on the surface of SBA-15 particles with most probably intergrain microporosity. The comparison of the N_2 sorption data of both series show that TiO_2 is more homogeneously dispersed in series b indicating that the presence of large mesopores is more favourable for the impregnation method used.

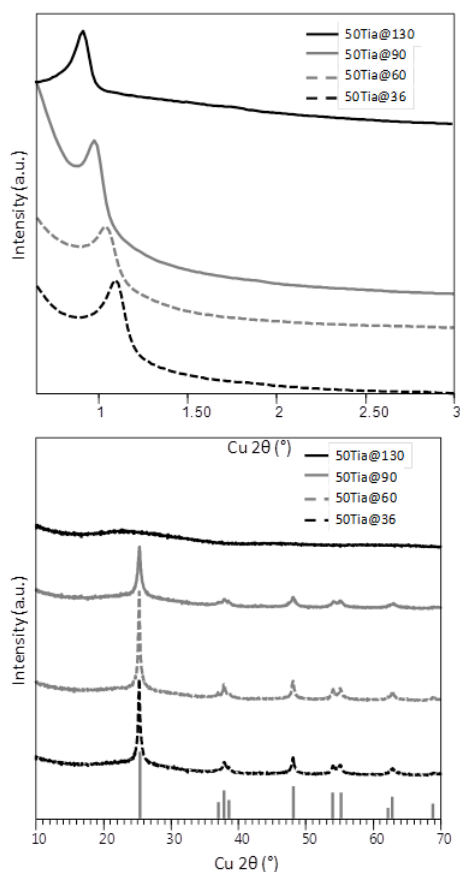


Fig. 6. Low (above) and wide (below) angle XRD patterns of the composites at 50% TiO_2 content (series a).

For the composites of series a prepared with 50 wt% of TiO_2 , the low angles XRD patterns exhibit the (1 0 0) diffraction peaks of the host supports in all cases. Compared to those of the host silica materials, the (1 0 0) peaks of corresponding composites are shifted to higher angles as a result of a network contraction upon the thermal treatment at 400 °C. The absence of the other reflexions is indicating of the loss of ordering probably due to the crystallization of TiO_2 during the thermal treatment at 400 °C. At wide angles, peaks corresponding to crystallized anatase (ICDD n°03-065-5714) are observed for composites prepared with SBA-15 aged at temperatures below 130 °C (Fig. 6). The absence of crystalline anatase on the XRD pattern of 50Tia@130 suggests that due to the large pores of the host, TiO_2 is entirely inside the porosity. According to the SEM images, the shape of N_2 adsorption/desorption isotherms

and XRD data it seems that with the SBA-15 aged at temperatures below 130 °C, the impregnation is both inside and outside the porosity where crystallized anatase is visible. By XRD Scherrer method, an average crystal size of 32, 43 and 18 nm is obtained for the composites with the supports aged at 36, 60 and 90 °C, respectively (Table 2). The crystal size is obviously much larger than the pore size confirming that anatase crystallized outside the SBA-15 host pores. By XRD quantification, the materials exhibit 19 wt% of anatase for 50Tia@90 and 22 wt% of anatase for 50Tia@36 and 50Tia@60. As no anatase reflection is visible for 50Tia@130 (Fig. 6), no quantification could be done. The results of anatase quantification and anatase crystal sizes of the different composites are summarized in Table 2.

Table 2: Crystal sizes and anatase amounts in the different composites with crystallized TiO_2

Sample	Crystal size ^a / nm	Anatase quantification ^b / wt%
50Tia@36	32	22
50Tia@60	43	22
50Tia@90	18	19
50Tib@130	8	15
70Tib@130	13	28
80Tib@130	23	44

^a average crystal size obtained using XRD Scherrer method

^b anatase quantification obtained by method described in the experimental part

Raman spectra of the composites of series a are presented Fig. 7. A sample of commercial anatase 10 nm was used as reference.

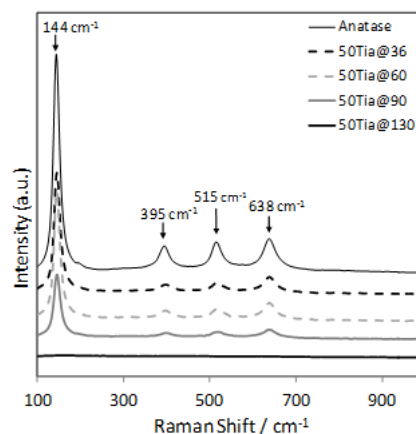


Fig. 7. Raman spectra of the composites of series a (50 wt% of TiO_2).

The four different bands at 144, 395, 515 and 638 cm^{-1} , assigned to crystallized anatase are visible for anatase 10 nm and all composites except for 50Tia@130. These results confirm that no crystallized anatase is present in 50Tia@130 sample. Composites of series a have been observed by TEM (Fig. 8 and S4). For each sample, the corresponding image obtained by dark field method is presented, allowing to bring out the crystallized TiO_2

particles. No visible crystallized particle is visible in 50Tia@130, which is in agreement with the results obtained by wide-angle XRD and Raman. For all samples, the lattice fringes corresponding to the packing of cylindrical mesopores of the silica SBA-15 hosts are clearly observed. In the case of 50Tia@36 and 50Tia@60, aggregates of particles of about 5nm in diameter are also observed on the surface of rod-shape SBA-15 particles (Fig. 8b). These particles are probably TiO_2 particles formed under thermal treatments at 400 °C. These observations are in agreement with SEM observations showing particles with undefined morphology. The TEM images with dark field mode show that crystalline anatase particles are well dispersed with a major proportion on the SBA-15 particle surface.

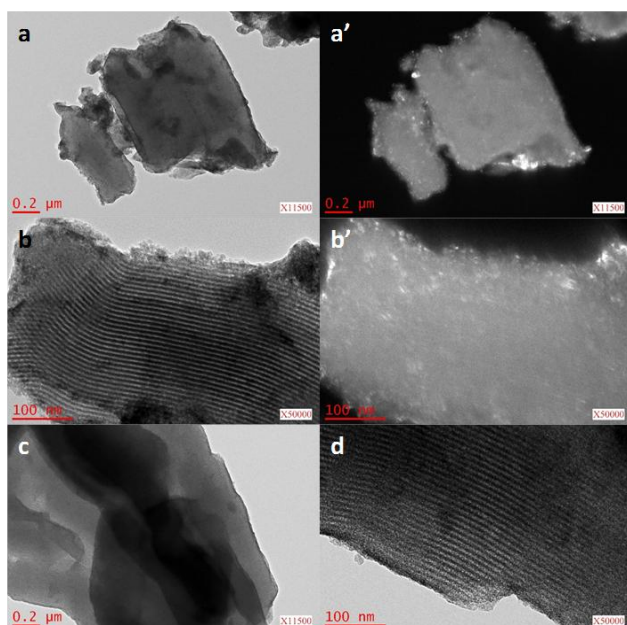


Fig. 8. TEM images of composites of series a: (a,a',b,b') 50Tia@36 and (c,d) 50Tia@130.

In the series b of composites, the same SBA-15 was used as host support and the TiO_2 quantity impregnated was varied. Fig. 9 presents low- and wide-angle XRD patterns of the composites of series b. For all composites at least the reflexion (1 0 0) is observed on low-angle XRD patterns. The (1 1 0) and (2 0 0) are also clearly observed for the composites with low TiO_2 contents, 10Tib@130 and 25Tib@130. However, these two reflexions are not observed at higher TiO_2 content (≥ 50 wt%), while they are clearly observed for a physical mixture of silica SBA-15 with crystalline anatase (50 wt%) (Fig. S5).

This confirms that at high TiO_2 contents the crystallisation of TiO_2 upon thermal treatment at 400 °C leads to significant structural changes. The decrease of the intensity of the reflexions is a consequence of the dilution of TiO_2 with silica SBA-15 matrix. The presence of crystallized anatase in the composites from 50 wt% of TiO_2 content is evidence by wide-angle XRD and Raman spectroscopy (Fig. 9 and 10).

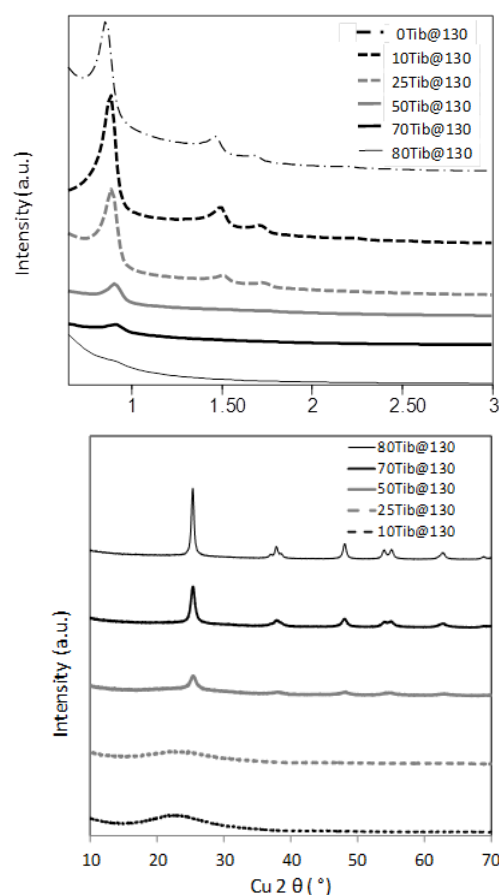


Fig. 9. Low angle (left) and wide angle (right) XRD patterns of the catalysts with different TiO_2 content (series b).

It is noteworthy that contrary to 50Tia@130, the composite 50Tib@130 presents some crystallized anatase. This can be explained by the small differences observed in textural properties of the two host supports used (Table 1). These differences reveal some problems of repeatability due to uncontrolled experimental parameters such as the addition way of SiO_2 and TiO_2 precursors and the room temperature during impregnation.

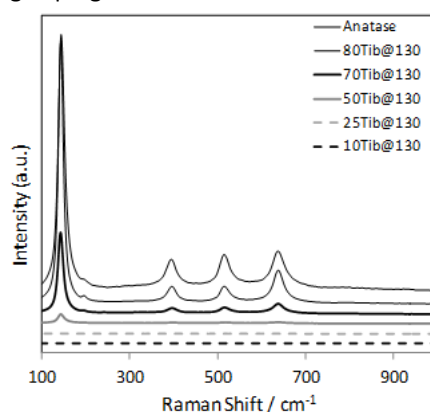


Fig.10. Raman spectra of the composites of series b

The presence of crystallized anatase in composites with 50, 70 and 80 wt% TiO_2 content is confirmed by TEM images with dark field mode presented Fig. 11 and S6.

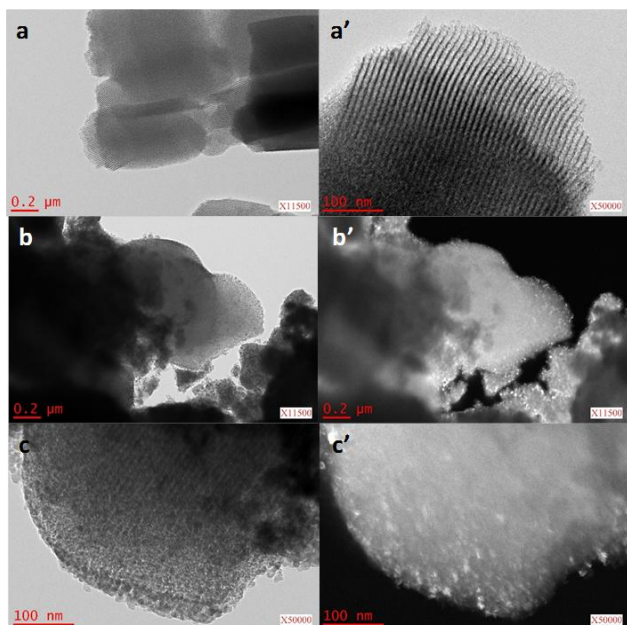


Fig. 11. TEM images of composites of series b: (a,a') 10Tib@130 and (b,b',c,c') 70Tib@130

There is no TEM images in dark field mode for 10Tib@130 and 25Tib@130 because no crystallized anatase is present in both samples, which is consistent with XRD and Raman results. For all samples, particles with rod-shape morphology and lattice fringes characteristics of the 2D-hexagonal pore network characteristic of the SBA-15 hosts are clearly observed. Like for 50Tia@36 and 50Tia@60, small 5-nm particles more or less aggregated are also observed on the SBA-15 particle surfaces of 50Tib@130, 70Tib@130 and 80Tib@130. These observations are consistent with SEM images. Anatase crystallites look homogeneous in size and homogeneously dispersed inside or outside the silica SBA-15 hosts. The crystal sizes measured by XRD Scherrer method on the samples are 8, 13 and 23 nm for the samples containing 50, 70 and 80 wt% of TiO_2 , respectively (Table 2).

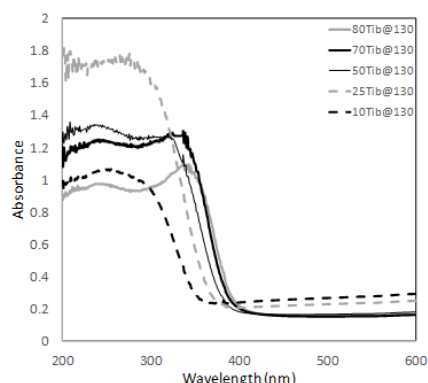


Fig. 12. Diffuse reflectance UV-Vis spectra of the series b composites.

When increasing the TiO_2 content, the impregnation and the crystallization of TiO_2 takes place inside and outside the porosity. By XRD quantification the materials exhibit 15, 28

and 44 wt% of crystallized anatase for 50, 70 and 80 wt% of TiO_2 content, respectively.

Fig.12 shows the Diffuse Reflectance UV-Vis spectra of the different composites of series b. The adsorption occurs in a range between 230 and 400 nm. They exhibit a broad band that can be decomposed in two parts. The first contribution at around 250 nm arises from a ligand to metal charge transfer transition in isolated TiO_4 units. It corresponds to coordinated Ti^{4+} species that are incorporated into the silica framework. The second contribution at 350 nm corresponds to small TiO_2 clusters. A blue shift is observed when the titania content decreases meaning that the size of the particles is reduced. This blue shift has been observed for titania nanoparticles^{57,58} on silica and corresponds to small TiO_2 clusters through the quantum size effect. These observations support the XRD results, i.e. an increase of the particles' size as a function of the TiO_2 content.

Using the Kubelka-Munk function, the band gap (E_g) has been calculated from a plot of $(\alpha hv)^2$ versus photon energy ($h\nu$), where α stands the adsorption coefficient. The band gap is determined by extrapolating the straight line portion of $(\alpha hv)^2 = 0$ axis. The intercept of the tangent of the plot gives the value of E (Fig. S7). The band gap decreases from 4.0 to 3.4 eV, when the TiO_2 content is increased from 10 to 80% (Fig13). Thus, with the increase of the titania content E_g is near the value of the pure anatase 3.2 eV. This result is in accordance with the ones obtained by XRD. Indeed it should be reminded that an increase of the anatase content in the composite is noted when the TiO_2 content varies from 10 to 80%.

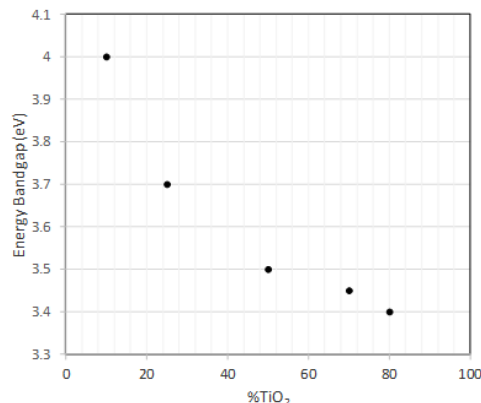


Fig. 13. Evolution of the energy band gap of the composites according to the TiO_2 content.

Photocatalysis experiments

Fig. 14 shows the photocatalytic results obtained using the catalysts of the series a compared to commercial anatase 10 nm and P25. P25 appears to be the best photocatalyst with a total degradation of MO after 90 min of irradiation time. With the host support synthesized at 130 °C the MO degradation is less important, only 20 % of degradation is observed after 150 min. This sample also corresponds to the one for which no crystallization of anatase was

ARTICLE

Journal Name

observed. For the other samples, the degradation profile is quite similar which can be explained by the presence of almost the same crystallized anatase amount (around 20 wt%).

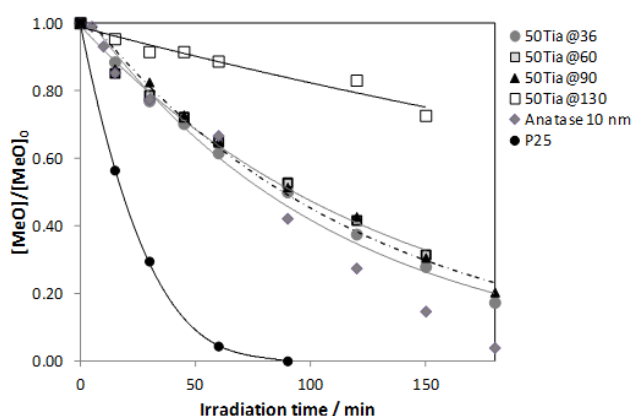


Fig. 14. Evolution of MO concentration with irradiation time by using the different catalysts at 50 wt% of TiO₂ (series a) and two commercial references.

Compared to the sample of anatase 10 nm, the profiles of the samples at 50 wt% of TiO₂ using SBA-15 host support aged at temperature inferior to 130 °C are quite similar until 90 min of reaction.

Moreover, the anatase 10 nm exhibits a better activity than the composites. The evolution of the MO concentration with the irradiation time using the samples at different TiO₂ contents prepared from SBA-15 silica aged at 130 °C (series b) as photocatalysts, is presented Fig. 15. In this case, it clearly appears that the degradation of MO using samples with low TiO₂ content (10 and 25 wt%) is quite low and slow. This is consistent with the absence of any crystallized anatase observed by wide-angle XRD. The necessity of having crystallized anatase particles is evidenced here, by comparing 50Ti@130 of both series (Fig. 14 and 15), the photoactivity is improved in the second case (series b – Fig. 15) when crystallized particles are present in the composite. Moreover, it seems that the degradation of MO is improved by increasing the TiO₂ content (Fig. 15). No relevant difference is observed between the samples with 70 or 80 wt% of TiO₂ but their photoactivity is very similar to that of anatase 10 nm. These results are interesting, since, although there is 70 or 80 wt% of TiO₂ due to the impregnation method, only a part of it had crystallized in anatase resulting in 28 and 44 wt % of anatase, respectively, with particle size of about 13 and 23 nm, respectively.

It is noteworthy that the commercial anatase 10 nm is totally crystallized (100 wt%) and in the same particle size range. In a previous study it was shown that at the same MO concentration the photodegradation rate depends on the catalyst content⁶⁰. Anatase nanocrystals appear thus more efficient photocatalysts when they are dispersed in silica matrices with high specific surface areas.

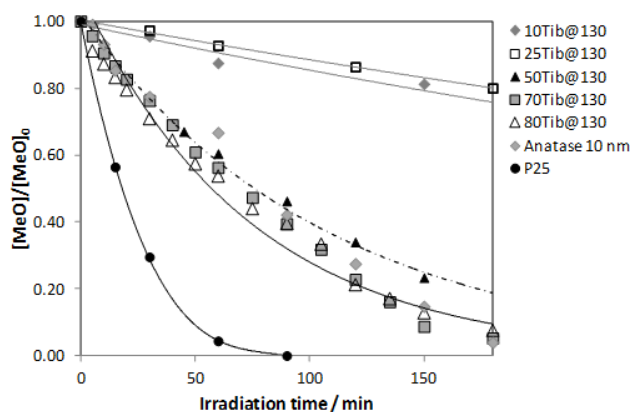


Fig. 15. Evolution of MO concentration with irradiation time by using the different catalysts at different wt% of TiO₂ (series b) and two commercial references.

However P25 appears to be the best catalyst for the MO degradation in our conditions. The unusual high photocatalytic activity of the TiO₂ P25 is attributed to the complex structure of this material since it is a mixture of anatase crystallites with amorphous and rutile phases. For nanoparticles (such as P25), the transportation length of electron/hole from crystal interface to the surface is short, which helps to accelerate the migration rate of electron/hole to the surface of the nanoparticle to participate the reaction process⁵⁹.

The commercial anatase 10 nm and 80Tib@130 are then the following best catalysts. But although, anatase 10 nm is better at the beginning of the degradation of MO, the composite 80Tib@130 tends to follow the same profile of anatase 10 nm after 100 min of irradiation, which confirms that with less crystallized anatase in the catalyst (44 wt%), the composite exhibits a photocatalytic activity close to the fully crystallized anatase one.

The effect of the anatase concentration on the degradation rate of MO is evaluated Fig. 16. The rates are determined at 60 min after the initiation of the photocatalytic activities. This reaction time is high enough to obtain different values for the degradation rates under different conditions. The catalyst loading is the same for each experiment in order to avoid the photodegradation activity variations that can be observed⁶⁰.

By observing Fig. 16, it appears that anatase 10 nm sample and composites at 50 wt% of TiO₂ exhibit equivalent rates of degradation of MO. In the first case, anatase 10 nm exhibits 100 wt% of crystallized anatase whereas the 50 wt% composites exhibit around 20 wt% of crystallized anatase for the same quantity of catalyst. At this stage, the composites at 50 wt% composites exhibit identical rate degradation with lower crystallized anatase. These composites are clearly more efficient than anatase 10 nm. Moreover It is worth mentioning the important degradation rates obtained by the composites with 70 and 80 wt% of TiO₂, that are higher than the one with fully crystallized sample and the best degradation rate was observed using 80Tib@130 composite. In this case, the degradation rate of 80Tib@130, composite containing 44 % of anatase, is twice better than the anatase 10 nm one where the sample is

totally crystallized. It clearly appears that the composites synthesized in this study are better photocatalysts, when crystallized anatase nanoparticles are formed on SiO₂ surface during calcinations, than fully crystallized anatase nanoparticles.

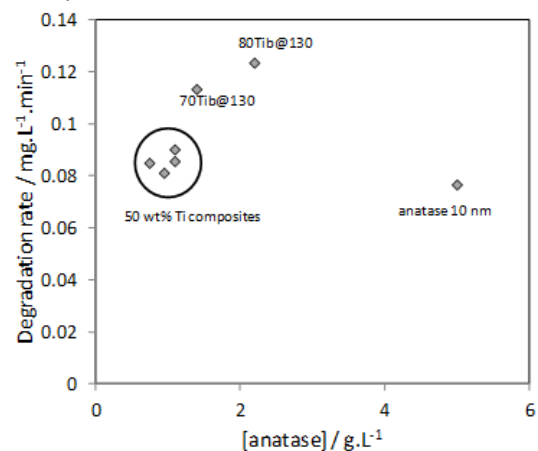


Fig. 16. Effect of the anatase content in the composites on the rate of degradation of MO.

Conclusions

Two different series of TiO₂-SiO₂ composites were synthesized by TiO₂ post-impregnation of a SBA-15 host supports. In series a, four SBA-15 supports with different pore sizes were prepared at different synthesis temperatures (36 °C, 60 °C, 90 °C and 130 °C) and the TiO₂ content was set at 50wt%. The influence of the pore size of the silica supports on the dispersion of TiO₂ was evidenced. A quasi-total impregnation of TiO₂ inside the porosity was observed for the SBA-15 with large mesopores of about 8 nm (synthesized at 130°C), and no crystalline anatase was observed by XRD and Raman. When mesopores are smaller, impregnation occurred inside and outside the porosity of the hosts and TiO₂ crystallized as anatase nanoparticles on the SBA-15 particle surface.

In series b, SBA-15 synthesized at 130 °C was used as host support and the TiO₂ content of the composites was varied from 10 to 80 wt%. In this series, when TiO₂ content was superior to 25wt%, the impregnation occurred both inside and outside the porosity, and TiO₂ crystallized in anatase nanoparticles outside the porosity. At low TiO₂ content (\leq 25wt%) the impregnation occurred homogeneously inside the mesopores and no crystalline anatase was observed by XRD and Raman. The use of SBA-15 host supports with large mesopores, compared to those used in series a, allows a better dispersion of TiO₂ particles. The quantity of crystallized anatase was determined by XRD using an internal standard when crystalline particles were detected. For these composites, the initial quantity of TiO₂ varied from 50 to 80 wt% has led to different quantities of crystallized anatase from 15 to 44 wt%, respectively.

The bandgap energy of the samples was estimated using diffuse reflectance spectroscopy. Results show that Eg

decreases with the increases of titania content, which affects the photoactivity of the composites. The photocatalytic activity of the composites was evaluated by following the degradation of MO and compared to commercial TiO₂ references. While P25 sample appeared to be the best photocatalyst for the degradation of MO in our conditions, the photoactivity of the other composites containing crystallized anatase were similar to that of fully crystallized commercial anatase with a particle size of the same order of magnitude. It clearly appeared that the composite 80Tib@130 with only 44 wt% of crystallized anatase, exhibits the highest MO degradation rate of both series.

Acknowledgements

Issam Naboulsi is warmly thanked for his help in photocatalysis experiments. Habiba Nouali and Ludovic Josien are thanked for the analyses made on the platforms (certified ISO9001) Adsorption and Electronic Microscopy, respectively, of IS2M.

References

- 1 J.M. Hermann, *Top. Catal.*, 2005, **34**, 49.
- 2 U.I. Gaya and A.H.Abdullah, *J. Photochem. Photobiol. C: Photochem. Rev.*, 2008, **9**, 1.
- 3 M. Andersson, L. Osterlund, S. Ljungstrom and A. Palmqvist, *J. Phys. Chem. B*, 2002, **106**, 10674.
- 4 X. Chen and S.S. Mao, *Chem. Rev.*, 2007, **107**, 2891.
- 5 A. Fujishima, X. Zhang and D. A. Tryk, *Surf. Sci. Reports*, 2008, **63**, 515.
- 6 E. Pelizzetti, C. Minero, E. Borgarello, L. Tinucci and N. Serpone, *Langmuir*, 1993, **9**, 2995.
- 7 B. Ohtani, Y. Ogawa and S. Nishimoto, *J. Phys. Chem. B*, 1997, **101**, 3746.
- 8 Z. Li, B. Hou, Y. Xu, D. Wu and Y. Sun, *J. Colloid Interface Sci.*, 2005, **288**, 149.
- 9 D.S. Kim, S.J. Han and S.Y. Kwak, *J. Colloid Interface Sci.*, 2007, **316**, 85.
- 10 K. Zimny, J. Ghanbaja, C. Carteret, M.J. Stébé and J.L. Blin, *New J. Chem.*, 2010, **34**, 2113.
- 11 K. Zimny, C. Carteret, M.J. Stébé and J.L. Blin, *J. Phys. Chem. C*, 2012, **116**, 6585.
- 12 K. Assaker, T. Benamor, L. Michelin, B. Lebeau, C. Marichal, M.J. Stébé and J.L. Blin, *Microporous Mesoporous Mater.*, 2015, **201**, 43.
- 13 R. Zhang, A.A. Elzatahry and S.S. Al-Deyab, *Nano Today*, 2012, **7**, 344.
- 14 G. Xu, Z. Zheng, Y. Wu and N. Feng, *Ceramics Inter.*, 2009, **35**, 1.
- 15 M. Harada, T. Sasaki, Y. Ebina and M. Watanabe, *J. Photochem. Photobiol. A: Chem.*, 2002, **148**, 273.
- 16 J. Chen, F. Qiu, W. Xu, S. Cao and H. Zhu, *Appl. Catal. A: General*, 2015, **495**, 131.
- 17 M. Bonne, S. Pronier, Y. Batonneau, F. Can, X. Courtois, S. Royer, P. Marécot and D. Duprez, *J. Mater. Chem.*, 2010, **20**, 9205.
- 18 D.J. Reidy, J.D. Holmes and M.A. Morris, *Ceramics Inter.*, 2006, **32**, 235.
- 19 C. Galacho, M.M.L. Ribeiro Carrott and P.J.M. Carrott, *Microporous Mesoporous Mater.*, 2007, **100**, 312.
- 20 G. Li and X.S. Zhao, *Ind. Eng. Chem. Res.*, 2006, **45**, 3569.

- 21 J.A. Melero, J.M. Arsuaga, P. De Frutos, J. Iglesias, J. Sainz and S. Blázquez, *Microporous Mesoporous Mater.*, 2005, **86**, 364.
- 22 W.-H. Zhang, J. Lu, B. Han, M. Li, J. Xiu, P. Ying and C. Li, *Chem. Mater.*, 2002, **14**, 3413.
- 23 Y. Chen, Y. Huang, J. Xiu, X. Han and X. Bao, *Appl. Catal., A*, 2004, **273**, 185.
- 24 M.D. Alba, Z.H. Luan and J. Klinowski, *J. Phys. Chem.*, 1996, **100**, 2178.
- 25 J. Li, C. Zhou, H. Xie, Z. Ge, L. Yuan and X. Li, *J. Nat. Gas Chem.*, 2006, **15**, 164.
- 26 F. Bérubé, B. Nohair, F. Kleitz S. Kaliaguine, *Chem. Mater.*, 2010, **22**, 1988.
- 27 N.B. Lihitkar, M.K. Abyaneh, V. Samuel, R. Pasricha, S.W. Gosavi and S.K. Kulkarni, *J. Colloid. Interface Sci.*, 2007, **314**, 310.
- 28 S.G. Zhang, Y. Fujii, H. Yamashita, K. Koyano, T. Tatsumi and M. Anpo, *Chem. Lett.*, 1997, **26**, 659.
- 29 T. Maschmeyer, F. Rey, G. Sankar and J.M. Thomas, *Nature*, 1995, **378**, 159.
- 30 K. Yamagishi, S. Namba and T. Yashima, *Stud. Surf. Sci. Catal.*, 1991, **60**, 171.
- 31 G. Li, and X.S. Zhao, *Ind. Eng. Chem. Res.*, 2006, **45**, 3569.
- 32 J.L. Blin, M.J. Stébé and T. Roques-Carmes, *Colloids Surf. A Physicochem. Eng. Asp.*, 2012, **407**, 177.
- 33 K. Assaker, C. Carteret, T. Roques-Carmes, J. Ghanbaja, M.J. Stébé and J.L. Blin, *New J. Chem.*, 2014, **38**, 2081.
- 34 M. Bellardita, M. Addamo, A. Di Paola, L. Palmisano, L. Cassar and M. Borsa, *J. Hazard. Mater.*, 2010, **174**, 707.
- 35 T. Cetinkaya, L. Neuwirthová, K.M. Kutláková and V. Tomášek, *Appl. Surf. Sci.*, 2013, **279**, 384.
- 36 K.Y. Jung and S.B. Park, *Appl. Catal. B: Environment.*, 2000, **25**, 249.
- 37 M.T. Nguyen Dinh, P. Rajbhandari, C. Lancelot, P. Blanchard, C. Lamonier, M. Bonne, S. Royer, F. Dumeignil and E. Payen, *ChemCatChem*, 2014, **6**, 328.
- 38 A. Corma, M.T. Navarro and J. Perez-Pariente, Patent 930 132 7 1993,
- 39 A. Corma A, M.T. Navarro and J. Perez-Pariente, *J Chem Soc. Chem. Commun*, 1994, **2**, 14718.
- 40 M. Morey, A. Davidson and G. Stucky, *Microporous Mater.*, 1996, **6**, 99.
- 41 D.Y. Zhao, Q.S. Huo, J.L. Feng, B.F. Chmelka and G.D. Stucky, *J Am Chem Soc.*, 1998, **120**, 6024.
- 42 P.T. Tanev, M. Chibwe and T.J. Pinnavaia, *Nature*, 1994, **368**, 321.
- 43 A. Tuel and L.G. Hubert Pfalzgraf, *J. Catal.*, 2003, **217**, 343.
- 44 F. Chiker, J. Ph Nogier, F. Launay and J.L. Bonardet, *Appl. Catal. A*, 2003, **243**, 309.
- 45 Z. Luan, J.Y. Bae and L. Kevan, *Microporous Mesoporous Mater.*, 2001, **48**, 189.
- 46 M.V. Landau, L. Vradman, X. Wang and L. Titelman, *Microporous Mesoporous Mater.*, 2005, **78**, 117
- 47 A.A. Ismail and D.W. Bahnemann, *J. Mater. Chem.*, 2011, **21**, 11686.
- 48 J. Yang, J. Zhang, L. Zhu, S. Chen, Y. Zhang, Y. Tang, Y. Zhu and Y. Li, *J. Hazard. Mater. B*, 2006, **137**, 952.
- 49 W.-T. Qiao, G.-W. Zhou, X.-T. Zhang and T.-D. Li, *Materials Sc. Engin. C*, 2009, **29**, 1498.
- 50 W. Wang and M. Song, *Microporous Mesoporous Mater.*, 2006, **96**, 255.
- 51 M.-J. López-Muñoz, R. van Grieken, J. Aguado and J. Marugán, *Catal. Today*, 2005, **101**, 307.
- 52 X. Qian, K.Fuku, Y. Kuwahara, T. Kamegawa, K. Mori and H. Yamashita, *ChemSusChem*, 2014, **7**, 1495.
- 53 D. Zhao, J. Feng, Q. Huo, N. Melosh, G.H. Fredrickson, B.F. Chmelka and G.D. Stucky, *Science*, 1998, **279**, 548.
- 54 C.P. Jarionec, M. Kruk and M. Jarionec, *J. Phys. Chem. B*, 1998, **102**, 5503.
- 55 K.S.W. Sing, *Pure Appl. Chem.*, 1985, **57**, 603.
- 56 A. Galarneau, H. Cambon, F. Di Renzo, R. Ryoo, M. Choi and F. Fajula, *New J. Chem.*, 2003, **27**, 73.
- 57 X. Gao, S.R. Bare, J.L.G. Fierro, M.A. Banares and I.E. Wachs, *J. Phys. Chem. B*, 1998, **102**, 5653.
- 58 B.J. Aronson, C.F. Blanford and A. Stein, *Chem. Mater.*, 1997, 2842.
- 59 D. Beydoun, R. Amal, G. Low and S. McEvoy, *J. Nanoparticle Res.*, 1999, **1**, 439.
- 60 J.L. Blin, M.J. Stébé and T. Roques-Carmes, *Coll and surfaces A: Physisorption Eng Aspects*, 2012, **407**, 177.



Journal Name

ARTICLE

New Journal of Chemistry Accepted Manuscript



Journal Name

ARTICLE

Influence of the porous texture of SBA-15 mesoporous silica on the anatase formation in $\text{TiO}_2 - \text{SiO}_2$ nanocomposites

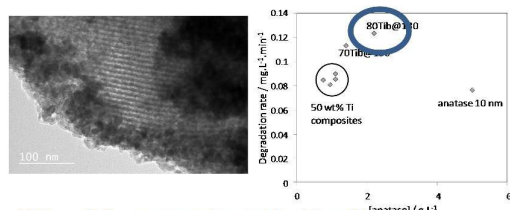
Received 00th January 20xx,
Accepted 00th January 20xx

DOI: 10.1039/x0xx00000x

www.rsc.org/

Manon Besançon,^a Laure Michelin,^a Ludovic Josien,^a Loïc Vidal,^a Karine Assaker,^b Magali Bonne,^{*a}
Bénédicte Lebeau,^{*a} Jean-Luc Blin^b

Table of Contents of manuscript ID: NJ-ART-10-2015-002859



$\text{TiO}_2 - \text{SiO}_2$ composite with 44 wt% of anatase exhibits a better MO degradation rate than fully crystallized anatase

New Journal of Chemistry Accepted Manuscript